

# Development of Numerical Methods for the Simulation of Compressible Droplet Dynamics Under Extreme Ambient Conditions



Steven Jöns, Stefan Fechter, Timon Hitz, and Claus-Dieter Munz

**Abstract** The computation of two-phase flow scenarios in a high pressure and temperature environment is a delicate task, for both the physical modeling and the numerical method. In this article, we present a sharp interface method based on a level-set ghost fluid approach. Phase transition effects are included by the solution of the two-phase Riemann problem at the interface, supplemented by a phase transition model based on classical irreversible thermodynamics. We construct an exact Riemann solver, as well as an approximate Riemann solver. We compare numerical results against molecular dynamics data for an evaporation shock tube and a stationary evaporation case. In both cases, our numerical method shows a good agreement with the reference data.

## 1 Introduction

To accurately predict phase transition in fluid flows with high pressure and temperature, e.g., nozzles and rocket combustion chambers, several obstacles need to be overcome. On the one hand, the lack of thermodynamic equilibrium necessitates sophisticated models for the phase transition process. Thereby, one needs to consider the microscale nature of the transition from a liquid to a vapor and the macroscopic impact on the surrounding fluid flow. On the other hand, if the pressures and temperatures are in the vicinity of the critical point, the compressibility of both fluids can not be neglected.

In the collaborative research council *SFB-TRR75*, a numerical framework for this scenario was developed in subproject *TP-A2*. The first and second funding period laid the groundwork in close cooperation with *TP-A3*: a sharp interface level-set ghost fluid method [14]. In this method, the grid size is assumed to be much larger than the width of the interfacial transition zone. Therefore, the interface is approximated as a discontinuity. The phases are treated individually from each other, while suitable

---

S. Jöns (✉) · S. Fechter · T. Hitz · C.-D. Munz

Institute of Aerodynamics and Gas Dynamics (IAG), University of Stuttgart, Stuttgart, Germany  
e-mail: [joens@iag.uni-stuttgart.de](mailto:joens@iag.uni-stuttgart.de)

© The Author(s) 2022

K. Schulte et al. (eds.), *Droplet Dynamics Under Extreme Ambient Conditions*,  
Fluid Mechanics and Its Applications 124,

[https://doi.org/10.1007/978-3-031-09008-0\\_3](https://doi.org/10.1007/978-3-031-09008-0_3)

jump conditions at the interface ensure the correct physical coupling. The bulk phases are treated with a discontinuous Galerkin spectral element method (DGSEM) [4, 23, 32] and real gas equations of state [17, 22]. The computationally efficient high-order DGSEM scheme can resolve fine details in the fluid flow. The use of a finite-volume sub-cell shock capturing [43] allows simulating the classical phenomena in compressible gas dynamics, e.g., shock waves. The position of the phase interface is captured by a level-set method, which is also treated via the DGSEM. The coupling of the two phases is done by applying a ghost fluid method [16, 37], in which the ghost states are defined from a Riemann solver. Two-phase Riemann solvers were proposed within the *SFB-TRR75* by Fechter et al. [12, 15]. They included considerations on evaporation, valid under isothermal conditions.

During the third funding period of the *SFB-TRR75*, the work of *TP-A2* focussed on evaporation in non-isothermal conditions. This was a challenging task, as the complicated thermodynamic mechanisms and the non-linear energy equation quickly lead to instabilities in the numerical scheme if the modelling of the evaporation process is not accurate. To gain more insight into the compressible evaporation process, a fruitful cooperation with *TP-B6* was started. By comparing molecular dynamics data from *TP-B6* with solutions of the authors sharp-interface method in [24, 25], a strategy was developed to validate different evaporation models. Thereby, the method of Hitz et al. [25] was constructed, that was able to simulate a non-isothermal shock tube scenario with evaporation. Deviations from the molecular dynamics data of *TP-B6* were limited to the temperature profile. Discussions of related scenarios exist in literature by the experiments of Simões-Moreira and Shepherd [42]. However, a description of the observed evaporation was only possible with a mixture approach. Le Métayer successfully made use of the Chapman-Jouguet theory in [34], though this approach is limited to the case of the maximum possible mass flux, which strongly simplifies the thermodynamic consideration. The method developed in *TP-A2* on the other hand, is a more general approach, applicable to any subcritical evaporation scenario when the appropriate material parameters are known.

Further work in the third funding period were related to improvements in the sharp-interface method for accurate simulations of droplet dynamics, including merging phenomena, c.f., [30, 38]. The numerical framework of *TP-A2* was used in cooperation with *TP-B5* to investigate bubble growth in a superheated liquid [9, 10]. Similar, a diffuse interface method, based on the Navier–Stokes Korteweg Equations, was developed together with *TP-A3* [26].

In this article, we focus on the building blocks for a non-isothermal evaporation model that were developed in the third funding period. We build on the results achieved in Hitz et al. [25] and propose a novel thermodynamic closure for the conditions at the interface, based on classical irreversible thermodynamics. We formulate two different Riemann solvers and compare results of the sharp interface method against molecular dynamics data for the evaporation shock tube scenario from [25] as well as a stationary evaporation case from *TP-B6* [21].

The article is structured as follows. In Sect. 2 we describe the governing equations, followed by a description of our numerical framework in Sect. 3. The evaporation model, as well as its inclusion into an exact and an approximate Riemann solver, are

discussed in Sect. 4. Afterwards, numerical results are presented in Sect. 5, followed by our conclusion.

## 2 Governing Equations

We consider a sharp interface setting of two pure phases without a mixing zone. Hence, the domain of interest  $\Omega$  is divided into a liquid region  $\Omega^L$  and a vapor region  $\Omega^V$ , separated by the interface which is described by the hypersurface  $\Gamma$ . It is infinitesimally thin and neither carries mass, nor energy.

### 2.1 Conservation Equations

The two regions  $\Omega_L$  and  $\Omega_V$  are each governed by its own set of compressible Euler equations with heat conduction:

$$\mathbf{U}_t + \nabla \cdot \mathbf{F}(\mathbf{U}) = 0, \quad \text{with } \mathbf{U} = \begin{pmatrix} \rho \\ \rho \mathbf{v} \\ \rho e \end{pmatrix} \quad \text{and} \quad \mathbf{F}(\mathbf{U}) = \begin{pmatrix} \rho \mathbf{v} \\ \rho \mathbf{v} \otimes \mathbf{v} + \mathbf{I}p \\ \mathbf{v}(\rho e + p) + \mathbf{q} \end{pmatrix}, \quad (1)$$

where  $\rho$  denotes the density,  $\mathbf{v} = (u, v, w)^T$  the velocity vector,  $p$  the pressure,  $e$  the specific total energy, and  $\mathbf{q}$  the heat flux vector. We model the heat flux by Fourier's law

$$\mathbf{q} = -\lambda \nabla T, \quad (2)$$

where  $T$  is the temperature and  $\lambda$  is the thermal conductivity. The total energy of the fluid  $\rho e$  is composed of the internal energy  $\rho \epsilon$  and the kinetic energy:

$$\rho e = \rho \epsilon + \frac{1}{2} \rho \mathbf{v} \cdot \mathbf{v}. \quad (3)$$

### 2.2 Equation of State

In each fluid, pressure and specific internal energy are linked via an appropriate equation of state (EOS). Within our framework, algebraic, as well as multiparameter EOS, can be used. The tabulation technique of Föll et al. [17] ensures efficiency. In this paper, we rely on multiparameter EOS given in the form of the reduced Helmholtz energy:

$$\frac{\psi(\rho, T)}{\mathcal{R}T} = F^0(\delta, \theta) + F^r(\delta, \theta), \quad (4)$$

with  $\mathcal{R}$  denoting the specific gas constant,  $\delta = \rho/\rho_c$  the reduced density,  $\theta = T_c/T$  the inverse reduced temperature,  $F^0$  the ideal gas contribution of the reduced Helmholtz energy, and  $F^r$  the residual contribution. The main benefit of using EOS in this form is given by the fact that all other thermodynamic properties can be derived by exact differentiation of Eq. (4).

### 2.3 Interface Capturing

The position of the phase interface is implicitly given by the root of a level-set function  $\phi(\mathbf{x})$ , following [44]. From the level-set field, geometrical properties, e.g. the interface normal vector  $\mathbf{n}^{\text{LS}}$  and the interface curvature  $\kappa$  can be calculated [30]. The level-set transport equation

$$\phi_t + \mathbf{v}^{\text{LS}} \cdot \nabla \phi = 0, \quad (5)$$

describes the transport of  $\phi$  by a velocity-field  $\mathbf{v}^{\text{LS}}$ . Since  $\mathbf{v}^{\text{LS}}$  is obtained from the interface conditions, this velocity needs to be extrapolated into the remaining domain by solving the Hamilton-Jacobi equations

$$\frac{\partial v_i^{\text{LS}}}{\partial \tau} + \text{sign}(\phi) \mathbf{n}^{\text{LS}} \cdot \nabla v_i^{\text{LS}} = 0, \quad (6)$$

with the direction-wise components  $v_i^{\text{LS}}$  of the velocity field  $\mathbf{v}^{\text{LS}}$  and the pseudo time  $\tau$ , following [2].

Ideally, the level-set function fulfills the signed distance property. However, Eq. (5) does not preserve it. Hence, the level-set function needs to be reinitialized. Following [44], we use the Hamilton-Jacobi equation

$$\phi_t + \text{sign}(\phi) (|\nabla \phi| - 1) = 0, \quad (7)$$

to retain the signed distance property. The solutions of Eqs. (5)–(7) are only necessary in a narrow band encompassing the interface. Outside this narrow band, the level-set function is set to the bands fixed radius and the velocity field is set to zero.

## 3 Numerical Methods

In the following, we describe our numerical framework, which is based on the papers [13, 14, 30, 38]. The domain of interest  $\Omega$  is discretized into  $n_{\text{Elements}}$  non-overlapping hexahedral elements  $\Omega_e$ , with  $e = 1, \dots, n_{\text{Elements}}$ . The computational mesh is used as a baseline for both the conservation equations as well as level-set specific equations.

### 3.1 Conservation Equations

The conservation equations are discretized by the discontinuous Galerkin spectral element method (DGSEM) [31] with finite-volume sub-cells [39, 43]. In the high-order DGSEM, the ansatz function for the state and the flux is a polynomial of degree  $N$

$$\mathbf{U}_h(\mathbf{x}, t) = \sum_{i,j,k=0}^N \hat{\mathbf{U}}_{ijk}(t) \ell_{ijk}(\mathbf{x}) \quad \text{and} \quad \mathbf{F}_h(\mathbf{x}, t) = \sum_{i,j,k=0}^N \hat{\mathbf{F}}_{ijk}(t) \ell_{ijk}(\mathbf{x}), \quad (8)$$

with  $\ell_{ijk}$  being the polynomial basis function given by the tensor product of one-dimensional Lagrange polynomials. The weak formulation of the governing equations

$$\frac{\partial}{\partial t} \int_{\Omega_e} \mathbf{U}_h \ell_{ijk} d\mathbf{x} + \oint_{\partial\Omega_e} \hat{\mathbf{F}}^* \cdot \mathbf{n} \ell_{ijk} ds - \int_{\Omega_e} \mathbf{F}_h \cdot \nabla \ell_{ijk} d\mathbf{x} = 0, \quad (9)$$

is solved, where  $\mathbf{n}$  denotes the outward pointing normal vector of the element boundary and  $\hat{\mathbf{F}}^*$  a numerical flux function that couples neighbouring elements with each other. The integrals in Eq. (9) are solved by Gaussian quadrature using the same set of  $N + 1$  Gauss-Legendre points as in the polynomial ansatz. Solution gradients, e.g. of the temperature, can be calculated by applying the BR1 lifting procedure [3]. Details on the implementation can be found in [4, 23, 32].

As the DGSEM is a high-order method, discontinuities, e.g., shocks and phase boundaries, will ultimately lead to the appearance of the unwanted Gibbs phenomena. To stabilize the solution in these areas, we combine the DGSEM with a finite-volume (FV) sub-cell method following [43]. Areas, in which sub-cells are needed, are identified by a modal indicator [39] for shocks and the position of the level-set root for the interface. In the respective elements, the solution representation is switched from a polynomial of degree  $N$  to  $N + 1$  equidistantly spaced FV sub-cells. This switch is conservative because of

$$\int_{\Omega_e} \mathbf{U} d\mathbf{x} \equiv \int_{\Omega_e} \mathbf{U}_{DG} d\mathbf{x} = \int_{\Omega_e} \mathbf{U}_{FV} d\mathbf{x}. \quad (10)$$

The FV scheme in the sub-cells is extended to a second-order total variation diminishing (TVD) scheme with a minmod limiter. A correct coupling of the polynomial and FV solution is ensured, by using the FV representation for the flux calculation and then projecting to the polynomial discretization for the discontinuous Galerkin (DG) elements. Once elements are no longer troubled, i.e., the FV sub-cells are no longer necessary, the solution representation is switched back to the DG polynomial. Next to the stabilization of the DG scheme, the sub-cell approach locally refines the computational grid, improving the spatial localization of the strong gradient.

### 3.2 Interface Capturing

The level-set transport equation (5) is discretized with a DGSEM method for hyperbolic equations with non-conservative products [11, 30], using the framework of path-conservative schemes of [8]. As in the flow equations, the solution ansatz for the level-set function is a polynomial of degree  $N$

$$\phi_h(\mathbf{x}, t) = \sum_{i,j,k=0}^N \hat{\phi}_{ijk}(t) \ell_{ijk}(\mathbf{x}). \quad (11)$$

The weak formulation of Eq. (5) reads as

$$\frac{\partial}{\partial t} \int_{\Omega_e} \phi_h \ell_{ijk} d\mathbf{x} + \oint_{\partial\Omega_e} \mathbf{B}(\mathbf{x}) \cdot \nabla \phi_h \ell_{ijk} ds + \int_{\Omega_e} \mathbf{B}(\mathbf{x}) \cdot \nabla \phi_h \ell_{ijk} d\mathbf{x} = 0, \quad (12)$$

with  $\mathbf{B}(\mathbf{x}) = \mathbf{v}^{\text{LS}}$ . Herein, the path-conservative jump term  $\mathbf{B}(\mathbf{x}) \cdot \nabla \phi_h$  is approximated by a path-conservative Rusanov Riemann solver from [11].

Although the level-set function is by definition a smooth signed-distance function, in practical applications discontinuities may occur, e.g., at the edge of the narrow band or in the case of merging droplets. Therefore, the FV sub-cell approach is used for the level-set transport as well. For details on the path-conservative scheme and the FV shock-capturing we refer to [11] and [30]. In addition to the level-set transport, the two sets of Hamilton-Jacobi equations, (6) and (7) are each solved with a fifth-order WENO scheme [29] in combination with a third-order low storage Runge-Kutta method with three stages.

### 3.3 The Level-Set Ghost Fluid Method

The methods described above are the building blocks of our sharp interface method. A key component of an accurate simulation of interfacial flows is a correct coupling of the two phases. We follow the methodology presented in [37], with a Riemann solver based ghost fluid method. Therein, the solution of the Riemann Problem with the states left and right of the phase interface is constructed. Given the solution, the numerical flux at the interface can be calculated for each phase. We will detail the discussion on this topic in Sect. 4.2.

In our numerical framework, the solution is advanced in time by the following steps:

1. The level-set function is reinitialized.
2. Using the information given by the level-set function, the computational domain is decomposed into  $\Omega_L$  and  $\Omega_V$ . The domain boundaries coincide with the finite volume sub-cells, creating a surrogate phase boundary.

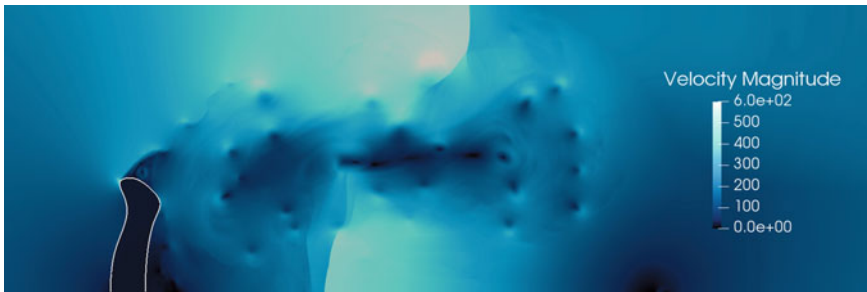


**Fig. 1** Velocity magnitude distribution of a 2D shock-drop interaction. The phase interface is depicted in white

3. Based on modal smoothness indicators and geometrical information of the level-set function, the DG-FV distribution of the fluid solution and the level-set function are updated.
4. Normal vector and curvature at the phase interface are calculated.
5. The two-phase Riemann problem is solved at the interface, providing the boundary condition for each phase and the velocity of the phase boundary at the interface.
6. The interface velocity is extrapolated into the volume to obtain a velocity field for the level-set transport.
7. An explicit fourth-order Runge-Kutta (RK) scheme from [7] is used to advance the level-set function and the fluid solution for each phase in time.

Our numerical framework is capable of predicting complex two-phase flow cases. Without phase transition and with slight modifications to the algorithm detailed in [30], the prediction of colliding droplets, merging droplets and shock-drop interactions have been shown in [30, 38, 47]. The distribution of the velocity magnitude of such a shock-drop interaction is shown in Fig. 1. Here, a shock with a Mach number of  $M = 1.47$  impinged on an initially round water column with a Weber number of  $We = 12$ . The deformation of the water column, as well as the complex velocity field can be seen. For further details on the simulation we refer to [30]. In addition to the scenarios depicted above, bubble growth in a superheated liquid was also investigated with our numerical framework in [9, 10]. In the following, we focus on considering phase transition. Fechter et al. [15] started the modeling of phase transition in this context. It was further continued by Hitz et al. in [25]. In the following, we build on their work and propose a novel closure for the two-phase Riemann problem.

## 4 Evaporation in the Sharp Interface Framework

In our numerical method, phase transition effects are included via two fundamental building blocks: A thermodynamic consistent model of evaporation at an interface and a Riemann solver to solve the two-phase Riemann problem. We will first discuss

the former and then consider the transfer of this model to the solution of the two-phase Riemann problem.

#### 4.1 Complete Evaporation at an Interface

We consider complete evaporation, i.e., evaporation of a pure liquid into a pure vapor, in a reference frame normal to the interface. To ensure the conservation of mass, momentum and energy at an evaporating interface, the following jump conditions need to be upheld:

$$[[\dot{m}]] = 0, \quad (13)$$

$$\dot{m} [[\mathbf{v} \cdot \mathbf{n}^I]] + [[p]] = \Delta p, \quad (14)$$

$$\dot{m} \left[ \left[ \epsilon + \frac{p}{\rho} + \frac{1}{2}(\mathbf{v} \cdot \mathbf{n}^I - \zeta)^2 \right] \right] + [[\mathbf{q} \cdot \mathbf{n}^I]] = 0, \quad (15)$$

where  $\dot{m}$  denotes the evaporation mass flux,  $\mathbf{n}^I$  the normal vector of the interface,  $\Delta p$  is the surface tension force and  $\zeta$  the velocity of the interface. The jump brackets for an arbitrary quantity  $\alpha$  are defined as  $[[\alpha]] = \alpha_{\text{vap}} - \alpha_{\text{liq}}$ , with  $\alpha_{\text{vap}}$  and  $\alpha_{\text{liq}}$  being the value of  $\alpha$  at the interface on the side of the vapor and the liquid, respectively. It is necessary to include the heat flux in Eq. (15), in order to describe phase transition with the Euler equations, as was shown by Hantke and Thein in [18].

In addition to Eqs. (13)–(15), we consider the entropy jump condition at the phase interface

$$\dot{m} [[s]] + \left[ \left[ \frac{\mathbf{q} \cdot \mathbf{n}^I}{T} \right] \right] = \eta_\Gamma, \quad (16)$$

with the specific entropy  $s$ , the temperature  $T$ , and  $\eta_\Gamma$  the entropy production term at the interface. As was shown by Hitz et al. [25],  $\eta_\Gamma$  can be written as

$$\eta_\Gamma := -\dot{m} \left[ \left[ \frac{g}{T} + \frac{1}{2} \frac{(\mathbf{v} \cdot \mathbf{n}^I - \zeta)^2}{T} \right] \right] + \dot{j}_e \left[ \left[ \frac{1}{T} \right] \right], \quad (17)$$

with the specific Gibbs energy  $g$  and an interfacial energy flux  $\dot{j}_e = \dot{m}(h + \frac{1}{2}(\mathbf{v} \cdot \mathbf{n}^I - \zeta)^2) + \mathbf{q} \cdot \mathbf{n}^I$ . In order to fulfill the second law of thermodynamics, it must always hold

$$\eta_\Gamma \geq 0. \quad (18)$$

If the entropy production term  $\eta_\Gamma$  is non-vanishing then the system departs from thermodynamic equilibrium. Assuming that the local equilibrium hypothesis is still valid, the theory of classical irreversible thermodynamics (CIT) [35] can derive a thermodynamic consistent solution for this situation. The CIT was already used by Hitz et al. in [25], where the numerical treatment was supplemented by a subgrid



model to calculate the heat flux in the vicinity of the phase interface. We depart from this approach and define closure relations for both mass and energy fluxes, solely based on the CIT, similar to [6].

Starting from the entropy production at the interface as given by Eq. (17), one can identify two thermodynamic fluxes,  $\dot{m}$  and  $\dot{J}_e$ , and two thermodynamic forces,  $f_m = - \left[ \left[ \frac{g}{T} + \frac{1}{2} \frac{(\mathbf{v} \cdot \mathbf{n}' - \xi)^2}{T} \right] \right]$  and  $f_e = \left[ \left[ \frac{1}{T} \right] \right]$ . In systems where two thermodynamic fluxes of the same tensorial order arise in the entropy production term, one generally speaks of coupled transport phenomena. Typical examples for such processes are thermoelectricity and thermodiffusion [35]. In these cases, the interdependence between the two fluxes is not negligible. Following the CIT, we assume linear flux-force relations and define phenomenological equations for the mass and energy flux as

$$\dot{m} = L_{mm} f_m + L_{me} f_e, \quad (19)$$

$$\dot{J}_e = L_{em} f_m + L_{ee} f_e, \quad (20)$$

where  $L_{mm}$ ,  $L_{me}$ ,  $L_{em}$  and  $L_{ee}$  are the so-called Onsager coefficients. These are material parameters, and they may depend on local state variables but not on their respective thermodynamic force. Since all forces in Eq. (17) are even under time reversal, the cross coefficients need to uphold the Onsager reciprocal relation, namely

$$L_{me} = L_{em}. \quad (21)$$

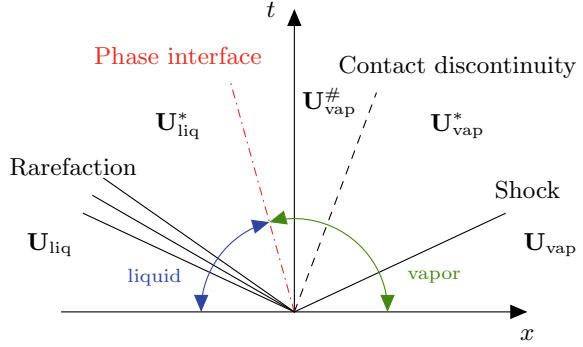
Based on kinetic theory, a few sets of models for the Onsager coefficients exist in the literature, see e.g., [5, 28]. However, they differ in their formulation of entropy production and are therefore currently not used in our framework. For the time, we restrict ourselves to the use of empirical fits.

## 4.2 Riemann Solvers for Evaporation

Given the evaporation model presented above, we can solve the two-phase Riemann problem at the interface. It is defined as an initial value problem with piecewise-constant initial states with, e.g., the left state being pure liquid and the right state pure vapor. As shown by the molecular dynamics data in [25], the solution of this type of Riemann problem adheres to the wave structure shown in Fig. 2. The outermost waves are classical non-linear waves, e.g., shock or rarefaction waves in the bulk phases. The inner waves are the classical contact discontinuity and the phase interface.

The phase interface appearing in the solution is not associated with any eigenvalue of the Euler equations and stems from the non-convexity of the EOS inside the spinodal region of the two-phase dome. For a problem with phase transition, the solution must find a path through the spinodal region, in which the hyperbolicity of the equations is lost. Menikoff and Plohr discussed the appearance of anomalous

**Fig. 2** Exemplary wave structure of the two-phase Riemann problem



wave structures when considering phase transition in [36]. They argue that the Euler equations do not include all relevant physical effects, leading to a non-uniqueness of the solution. The classical approaches to obtain a unique solution, like the Lax criterion or Liu’s entropy criterion, are not sufficient in this case.

To solve the problem of the non-uniqueness, we use the concept of a kinetic relation, initially proposed by Abeyaratne and Knowles [1]. The kinetic relation is a condition that provides the correct evaporation mass flux. In addition, it directly controls the entropy production at the interface. Following the framework of Rohde and Zeiler [40, 41] and its extension of Hitz et al. [25], we write the kinetic relation in the form

$$\mathcal{K}_{m,e} = \sum_i f_i J_i - G(\dot{m}, \dot{J}_e) = 0, \quad (22)$$

with  $f_i$ , and  $J_i$  being thermodynamic forces and fluxes, respectively;  $G(\dot{m}, \dot{J}_e)$  is a microscale measure of the entropy production. Using the phenomenological equations (19)–(20), one can derive the following kinetic relation:

$$\mathcal{K}_{m,e} = \dot{m} f_m + \dot{J}_e f_e - f_m (L_{mm} f_m + L_{me} f_e) - f_e (L_{em} f_m + L_{ee} f_e) = 0. \quad (23)$$

Equation (23) is an extension to the kinetic relation proposed by Hitz et al. [25]. However, the same conclusions can be drawn: Equation (23) is quadratic in both energy and mass flux and therefore very complex. A simplification is needed to ensure a successful incorporation into an iterative algorithm to solve the two-phase Riemann problem. The approach of Hitz et al. [25] was to assume an isothermal interface on a subgrid-level together with a subgrid model for heat transfer. We depart from this approach and simplify Eq. (23) by applying the CIT.

The kinetic relation governs the entropy production at the interface. This can either be done by directly comparing the macroscopic entropy production, given as the sum of the fluxes times the forces, or, with the microscopic entropy production, given by the phenomenological equations. In an alternative approach, one can define a kinetic relation of the form

$$\mathcal{K}_m = \dot{m} - L_{mm} f_m - L_{me} f_e = 0, \tag{24}$$

which directly controls the mass flux, by again comparing the macroscopic mass flux with the one predicted by the CIT. To ensure the correct entropy production at the interface, we calculate the heat fluxes such that the interfacial energy flux equals the one predicted by the CIT with Eq. (20). Thus, if  $\mathcal{K}_m$  is fulfilled, the entropy production at the interface is given by Eq. (17) and  $\mathcal{K}_{m,e}$  is naturally fulfilled as well.

Given Eq. (24), we proceed to discuss the Riemann solvers. In our numerical framework, two different approaches are available. First, an exact Riemann solver following Hitz et al. [25] as well as an approximate Riemann solver based on the work of Fechter et al. [15].

### 4.2.1 Exact Riemann Solver

The exact solver of Hitz et al. [25], originally based on the work of Fechter et al. [14], is able to resolve the full Riemann fan and thus find a solution of all three inner states. To ensure stability during the iteration process, an additional contact wave is included as shown in Fig. 3a. This procedure was proposed in [14, 48]. The additional contact wave is later removed once a solution has been found. The target function of the iteration scheme is defined by

$$\mathbf{G}_{TRP}(\tau_1, T_1, \tau_2, T_2, \tau_3, T_3, \tau_4, T_4) = (r_1, r_2, r_3, r_4, r_5, r_6, r_7, r_8)^T, \tag{25}$$

with  $\tau_i$  denoting the specific volume in the  $i$ th inner state and  $r_j$  the  $j$ th residual. The residuals  $r_1, \dots, r_5$  are defined by considering integral conservation across each of the classical waves. For details on these we refer to the publication of Hitz et al. [25]. The residuals  $r_6, r_7, r_8$  concern the conditions at the phase interface. These have been altered slightly with respect to the original method, in order to include the evaporation model described in Sect. 4.1. The residuals are given by the integral jump

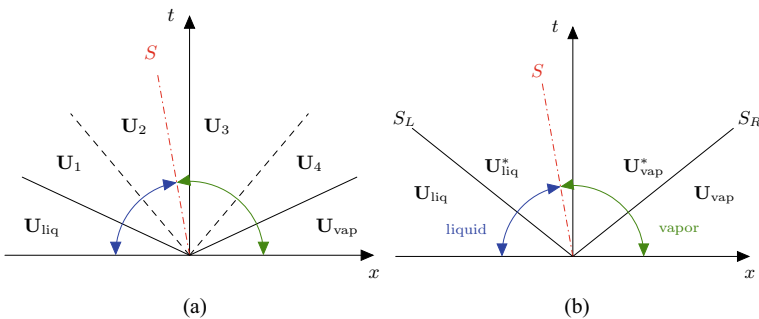


**Fig. 3** Wave fans of the Riemann solvers for the two-phase Riemann problem: **a** exact solver **b** HLLP solver

conditions for momentum and energy, as well as the kinetic relation and therefore read as

$$r_6 = \dot{m}(u_3 - u_2) + p_3 - p_2 - \Delta p \quad (26)$$

$$r_7 = \dot{m} \left( h_3 - h_2 + \frac{1}{2} \dot{m}^2 (\tau_3 - \tau_2) \right) + q_3 - q_2 \quad (27)$$

$$r_8 = \mathcal{K}_m. \quad (28)$$

The heat flux at the liquid side of the interface  $q_2$  is defined by ensuring the correct interfacial energy flux, given by Eq. (20):

$$q_2 = j_e - \dot{m} \left( h_2 + \frac{1}{2} \dot{m}^2 \tau_2 \right). \quad (29)$$

Since the thermal conductivity of the liquid is usually much higher than the thermal conductivity of the vapor phase, we assume that the heat of evaporation is predominantly provided by the liquid side and set

$$q_3 = 0. \quad (30)$$

We then solve the system  $\mathbf{G}_{TRP}$  with an eight-dimensional root-finding algorithm provided by the open-source libraries GSL(V2.1) and FGSL(V1.2.0). The solution of the Riemann problem provides the boundary conditions needed in the ghost fluid method. They are defined by the states left and right of the interface:

$$\hat{\mathbf{F}}_{\text{liq}}^* = \mathbf{F}_2 \quad \hat{\mathbf{F}}_{\text{vap}}^* = \mathbf{F}_3. \quad (31)$$

Note that the heat fluxes  $q_2$  and  $q_3$  are included in the flux.

#### 4.2.2 Approximate HLLP Riemann Solver

The downside of the exact solver is the immense computational cost due to the eight-dimensional root-finding algorithm. To reduce the complexity, we formulate an approximate HLLP Riemann solver, as proposed by Fechter et al. in [15]. Therein, the Riemann problem is solved for the simplified fan shown in Fig. 3b. This followed the ideas of the HLL and HLLC solver for single and multiphase situations [19, 27, 46]. The outer, non-linear waves are either shocks or rarefactions and the classical Rankine-Hugoniot jump conditions apply. The inner wave is the phase interface, for which the considerations from Sect. 4.1 are valid.

The solver is formulated as a one-dimensional iteration scheme, with the kinetic relation  $\mathcal{K}_m$  as the target function. Initially, the outer wave speeds are estimated by using

$$S_L = u_{\text{liq}} - a_{\text{liq}} \quad (32)$$

$$S_R = u_{\text{vap}} + a_{\text{vap}}, \quad (33)$$

with  $a$  being the speed of sound of the respective phase. Afterwards, the iteration procedure starts by calculating the inner states. They are given by a thermodynamically overdetermined state vector. The hydrodynamic components of the state vector  $\rho^*$ ,  $\mathbf{v}^*$ , and  $p^*$  can be calculated from the mass and momentum jump conditions across all three waves. The explicit formulas have been reported in [15]. The specific total energy in the inner states can be then calculated from the energy jump conditions across the two outer waves. Finally, the liquid heat flux can be calculated from the CIT and the vapor heat flux by fulfilling the energy jump condition across the interface:

$$q_{\text{liq}} = \dot{J}_e - \dot{m} \left( h_{\text{liq}}^* + \frac{1}{2} \dot{m}^2 \frac{1}{\rho_{\text{liq}}^*} \right), \quad (34)$$

$$q_{\text{vap}} = q_{\text{liq}} + \dot{m} \left( e_{\text{liq}}^* - e_{\text{vap}}^* \right) + \left( p_{\text{liq}}^* \mathbf{v}_{\text{liq}}^* \cdot \mathbf{n}^I - p_{\text{vap}}^* \mathbf{v}_{\text{vap}}^* \cdot \mathbf{n}^I \right) \quad (35)$$

In contrast to the exact solver, a local evaluation of the approximate Riemann solution is not used to calculate the interface flux since it is only valid in an integral sense. Hence, the boundary conditions for the ghost fluid method are calculated from the integral consistency conditions:

$$\hat{\mathbf{F}}_{\text{liq}}^* = \mathbf{F}_{\text{liq}} + S_L (\mathbf{U}_{\text{liq}}^* - \mathbf{U}_{\text{liq}}), \quad \hat{\mathbf{F}}_{\text{vap}}^* = \mathbf{F}_{\text{vap}} + S_R (\mathbf{U}_{\text{vap}}^* - \mathbf{U}_{\text{vap}}). \quad (36)$$

## 5 Numerical Results

In this section, we validate our numerical scheme by comparing it with data obtained from molecular dynamics simulations of *TP-B6*. In all our test cases, we considered the Lennard-Jones truncated and shifted fluid (LJTS). For this fluid, highly accurate EOS are available [20, 45], which makes a one-to-one comparison of the macroscopic and microscopic methods possible. We validated this kind of comparison in [24], where a shock tube scenario with a supercritical liquid and supercritical vapor, as well as an expansion into vacuum, were considered. Furthermore, we discussed a shock tube scenario with evaporation [25]. There, our numerical scheme showed promising results, however, deviations from the molecular dynamics data could be observed in the temperature. To validate the evaporation shock tube presented above, we first revisit the evaporation shock tube presented in [25]. Afterwards, we show numerical results of a novel stationary evaporation case.

In all the results presented below, we have used the PeTS EOS [20] to simulate the LJTS fluid. The Onsager coefficients were set to  $L_{mm} = 1.05E - 2$ ,  $L_{me} = -0.6E - 2$  and  $L_{ee} = 0.8E - 2$  for both cases. For the thermal conductivity, the model of

Lautenschlaeger et al. [33] was used. All quantities were non-dimensionalized with respect to the reference length  $\sigma_{\text{ref}} = 1 \text{ \AA}$ , the reference energy  $\epsilon_{\text{ref}}/k_B = 1 \text{ K}$  and reference mass  $m_{\text{ref}} = 1 \text{ u}$  as follows

$$x = \frac{\hat{x}}{\sigma_{\text{ref}}}, \quad t = \frac{\hat{t}}{\sigma_{\text{ref}} \sqrt{m_{\text{ref}}/\epsilon_{\text{ref}}}}, \quad \rho = \frac{\hat{\rho}}{m_{\text{ref}}/\sigma_{\text{ref}}^3}, \quad u = \hat{u} \sqrt{m_{\text{ref}}/\epsilon_{\text{ref}}}, \quad T = \frac{\hat{T}}{\epsilon_{\text{ref}}/k_B},$$

where the dimensional quantities are indicated with a hat. The polynomial degree of the DGSEM was set to  $N = 3$ . In the bulk phases, the HLLC-Riemann solver was used to calculate the numerical fluxes. For time integration, a fourth-order Runge-Kutta scheme with five stages was used. In the one-dimensional test cases presented below, we advect the computational mesh with the interface velocity using the ALE method for DGSEM, cf., [25]. Thus, the interface is kept sharp and does not move with respect to the grid.

## 5.1 Evaporation Shock Tube

The evaporation shock tube scenario is taken from [25]. It is a Riemann problem type-case with piecewise constant initial data:

$$\mathbf{U}(x, 0) = \begin{cases} \mathbf{U}_{\text{liq}} & \text{for } x < 0 \\ \mathbf{U}_{\text{vap}} & \text{for } x > 0. \end{cases} \quad (37)$$

The liquid is initially given in a saturated state with a temperature of  $T = 0.9$ . The vapor initially has a temperature of  $T = 0.8$  and a density of 50% of its saturation density. The computational domain  $x \in [-400, 1500]$  was discretized into 200 grid elements.

The numerical results for both Riemann solvers are shown in Fig. 4, supplemented by the molecular dynamics data from [25] for  $t = 600$ . The sharp interface method is capable of reproducing the reference data. In density, velocity, and temperature a qualitative and quantitative agreement can be seen, which is an improvement with respect to the results shown in [25]. The remaining differences between the molecular dynamics data and the sharp interface method may be explained by the lack of an appropriate model for the Onsager coefficients. At the shock wave, the absence of viscous effects can be seen as well. Between the two Riemann solvers, slight deviations can be observed in the vicinity of the interface, where the HLLP solver leads to a slightly cooler freshly evaporated vapor. However, the approximate Riemann solver reduces the total computational time by about 70% compared to the exact solver.

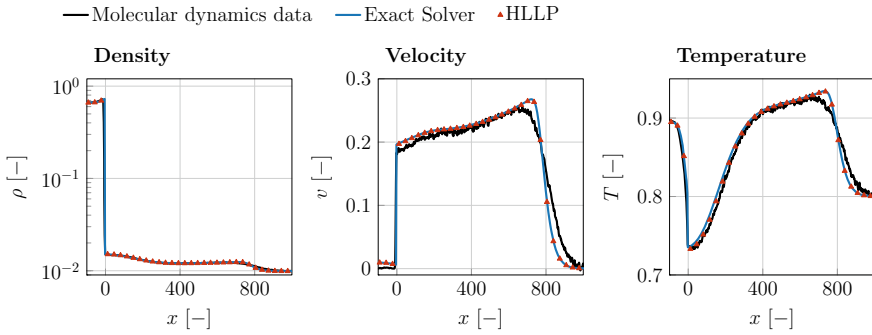


**Fig. 4** Evaporation shock tube with molecular dynamics data and results from the sharp interface method for different Riemann solvers

### 5.2 Stationary Evaporation

The stationary evaporation case is taken from the work of Heinen et al. [21]. It is less complex than the evaporation shock tube scenario described above since it only considers the sole interface. In this way, the modelling of the interface can be thoroughly investigated, as no other wave appears in the solution.

The domain is given by  $x \in [-12, 400]$ . The phase interface is positioned at  $x = 0$ . On the left boundary ( $x = -12$ ), liquid enters the domain at a temperature of  $T = 0.8$  and with a mass flux that equals the evaporation mass flux. On the other side ( $x = 400$ ), the velocity of the vapor is held constant at a value of  $u = 0.2$ . Initially, both liquid and vapor are saturated and have a temperature of  $T = 0.8$ . The liquid is at rest while the vapors initial velocity is  $u = 0.2$ . The simulation was run until  $t = 6000$ , where a stationary state was achieved. The domain was discretized with 100 elements and the HLLP solver was used as the interface solver.

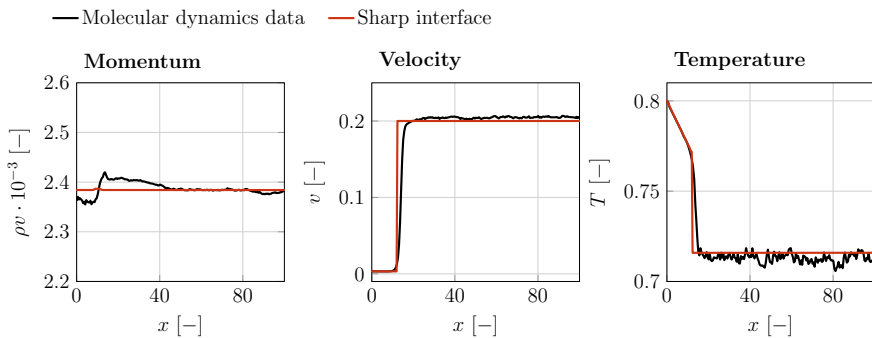


**Fig. 5** Comparison of molecular dynamics data and results by the sharp interface method for stationary evaporation case

Numerical results can be seen in Fig. 5, supplemented by the molecular dynamics data from [21]. In all three quantities, the sharp interface shows a very good agreement. Most notably, both the momentum and the temperature are predicted very well by our numerical method. We want to note that the same set of Onsager coefficients were chosen as in the evaporation shock tube case. Although only being an empirical fit against the data from [25], it shows accurate results for different test cases with a similar range of temperatures.

## 6 Conclusions

In this article, we surveyed the results of the subproject *TP-A2* within the Collaborative Research Center *SFB-TRR75*. The sharp interface method for droplet dynamics in high pressure and temperature environments and its extension to evaporation was considered. The method is based on a discontinuous Galerkin spectral element method, supplemented by finite-volume sub-cells. The interface tracking is done via a level-set method and the jump conditions across the phase interface are fulfilled via the use of special interface Riemann solvers. Evaporation is modeled via classical irreversible thermodynamics and linear constitutive laws. We discussed two different interface Riemann solvers: an exact solver which resolves the full wave fan of the two-phase Riemann problem, as well as an approximate HLLP Riemann solver with a reduced complexity of the wave fan.

Numerical results with the evaporation model were shown for an evaporation shock tube scenario as well as a stationary evaporation. Molecular dynamics data of *TP-B6* was used as a benchmark. In both cases, the numerical results showed a very good agreement with the reference data. The approximate Riemann solver showed only slight differences to the exact solver, while drastically reducing the computational effort.

The Onsager coefficients used in this work were fitted and not predicted by an appropriate model. Future investigations will focus on predictive models circumventing the need for an empirical fit. These shall be validated by a deepened discussion on the stationary evaporation for a variety of initial conditions in close cooperation with *TP-B6*. A comparison between our compressible framework and the incompressible one of *TP-B1* is planned as well. A next step will also be the use of our method in multi-dimensional applications.

**Acknowledgements** This work was supported by the German Research Foundation (DFG) through the Project SFB-TRR 75, Project number 84292822 - “Droplet Dynamics under Extreme Ambient Conditions”. The simulations were performed on the national supercomputer HPE Apollo (Hawk) at the High-Performance Computing Center Stuttgart (HLRS).



## References

1. Abeyaratne R, Knowles JK (1991) Kinetic relations and the propagation of phase boundaries in solids. *Arch Ration Mech Anal* 114(2):119–154. <https://doi.org/10.1007/BF00375400>
2. Aslam TD (2004) A partial differential equation approach to multidimensional extrapolation. *J Comput Phys* 193(1):349–355. <https://doi.org/10.1016/j.jcp.2003.08.001>
3. Bassi F, Rebay S (1997) A high-order accurate discontinuous finite element method for the numerical solution of the compressible Navier-Stokes equations. *J Comput Phys* 131(2):267–279. <https://doi.org/10.1006/jcph.1996.5572>
4. Beck AD, Bolemann T, Flad D, Frank H, Gassner GJ, Hindenlang F, Munz CD (2014) High-order discontinuous Galerkin spectral element methods for transitional and turbulent flow simulations. *Int J Numer Methods Fluids* 76(8):522–548
5. Bedeaux D, Kjelstrup S (1999) Transfer coefficients for evaporation 270:413–426
6. Bedeaux D, Kjelstrup S, Rubi JM (2003) Nonequilibrium translational effects in evaporation and condensation. *J Chem Phys* 119(17):9163–9170. <https://doi.org/10.1063/1.1613640>
7. Carpenter M, Kennedy C (1994) Fourth-order  $2N$ -storage Runge-Kutta schemes. Technical report, NASA Langley Research Center
8. Castro M, Gallardo J, Parés C (2006) High order finite volume schemes based on reconstruction of states for solving hyperbolic systems with nonconservative products. applications to shallow-water systems. *Math Comput* 75(255):1103–1134
9. Dietzel D, Hitz T, Munz CD, Kronenburg A (2019) Numerical simulation of the growth and interaction of vapour bubbles in superheated liquid jets. *Int J Multiph Flow* 121:103112. <https://doi.org/10.1016/j.ijmultiphaseflow.2019.103112>
10. Dietzel D, Hitz T, Munz CD, Kronenburg A (2019) Single vapour bubble growth under flash boiling conditions using a modified HLLC Riemann solver. *Int J Multiph Flow* 116:250–269. <https://doi.org/10.1016/j.ijmultiphaseflow.2019.04.010>
11. Dumbser M, Loubère R (2016) A simple robust and accurate a posteriori sub-cell finite volume limiter for the discontinuous Galerkin method on unstructured meshes. *J Comput Phys* 319:163–199. <https://doi.org/10.1016/j.jcp.2016.05.002>
12. Fechter S, Jaegle F, Schleper V (2013) Exact and approximate Riemann solvers at phase boundaries. *Comput Fluids* 75:112–126
13. Fechter S, Munz CD (2015) A discontinuous Galerkin-based sharp-interface method to simulate three-dimensional compressible two-phase flow. *Int J Numer Meth Fluids* 78(7):413–435
14. Fechter S, Munz CD, Rohde C, Zeiler C (2017) A sharp interface method for compressible liquid-vapor flow with phase transition and surface tension. *J Comput Phys* 336:347–374. <https://doi.org/10.1016/j.jcp.2017.02.001>
15. Fechter S, Munz CD, Rohde C, Zeiler C (2018) Approximate Riemann solver for compressible liquid vapor flow with phase transition and surface tension. *Comput Fluids* 169:169–185. <https://doi.org/10.1016/j.compfluid.2017.03.026>
16. Fedkiw RP, Aslam T, Merriman B, Osher S (1999) A non-oscillatory Eulerian approach to interfaces in multimaterial flows (the ghost fluid method). *J Comput Phys* 152(2):457–492. <https://doi.org/10.1006/jcph.1999.6236>
17. Föll F, Hitz T, Müller C, Munz CD, Dumbser M (2019) On the use of tabulated equations of state for multi-phase simulations in the homogeneous equilibrium limit. *Shock Waves*. <https://doi.org/10.1007/s00193-019-00896-1>
18. Hantke M, Thein F (2019) On the impossibility of first-order phase transitions in systems modeled by the full Euler equations. *Entropy* 21(11):1039. <https://doi.org/10.3390/e21111039>
19. Harten A, Lax PD, van Leer B (1983) On upstream differencing and Godunov-type schemes for hyperbolic conservation laws. *SIAM Rev* 25(1):35–61. <https://doi.org/10.1137/1025002>
20. Heier M, Stephan S, Liu J, Chapman WG, Hasse H, Langenbach K (2018) Equation of state for the Lennard-Jones truncated and shifted fluid with a cut-off radius of 2.5 sigma based on perturbation theory and its applications to interfacial thermodynamics. *Mol Phys* 116(15–16):2083–2094. <https://doi.org/10.1080/00268976.2018.1447153>

21. Heinen M, Vrabec J (2019) Evaporation sampled by stationary molecular dynamics simulation. *J Chem Phys* 151(4). <https://doi.org/10.1063/1.5111759>
22. Hempert F, Boblest S, Ertl T, Sadlo F, Offenhäuser P, Glass CW, Hoffmann M, Beck A, Munz CD, Iben U (2017) Simulation of real gas effects in supersonic methane jets using a tabulated equation of state with a discontinuous Galerkin spectral element method. *Comput Fluids* 145:167–179. <https://doi.org/10.1016/j.compfluid.2016.12.024>
23. Hindenlang F, Gassner GJ, Altmann C, Beck A, Staudenmaier M, Munz CD (2012) Explicit discontinuous Galerkin methods for unsteady problems. *Comput Fluids* 61:86–93. <https://doi.org/10.1016/j.compfluid.2012.03.006>
24. Hitz T, Heinen M, Vrabec J, Munz CD (2020) Comparison of macro- and microscopic solutions of the Riemann problem I. Supercritical shock tube and expansion into vacuum. *J Comput Phys* 402:109077. <https://doi.org/10.1016/j.jcp.2019.109077>
25. Hitz T, Jöns S, Heinen M, Vrabec J, Munz CD (2021) Comparison of macro- and microscopic solutions of the Riemann problem II. Two-phase shock tube. *J Comput Phys* 429:110027. <https://doi.org/10.1016/j.jcp.2020.110027>
26. Hitz T, Keim J, Munz CD, Rohde C (2020) A parabolic relaxation model for the Navier-Stokes-Korteweg equations. *J Comput Phys* 109714. <https://doi.org/10.1016/j.jcp.2020.109714>
27. Hu X, Adams N, Iaccarino G (2009) On the HLLC Riemann solver for interface interaction in compressible multi-fluid flow. *J Comput Phys* 228(17):6572–6589. <https://doi.org/10.1016/j.jcp.2009.06.002>
28. Jafari P, Masoudi A, Irajizad P, Nazari M, Kashyap V, Eslami B, Ghasemi H (2018) Evaporation mass flux: a predictive model and experiments. *Langmuir* 34(39):11676–11684. <https://doi.org/10.1021/acs.langmuir.8b02289>
29. Jiang GS, Peng D (2000) Weighted ENO schemes for Hamilton-Jacobi equations. *SIAM J Sci Comput* 21(6):2126–2143. <https://doi.org/10.1137/s106482759732455x>
30. Jöns S, Müller C, Zeifang J, Munz CD (2020) Recent advances and complex applications of the compressible ghost-fluid method. In: SEMA SIMAI Springer Series. Proceedings of Numhyp 2019. Springer accepted
31. Kopriva DA (2009) Spectral element methods. In: Scientific computation. Springer, The Netherlands, pp 293–354. [https://doi.org/10.1007/978-90-481-2261-5\\_8](https://doi.org/10.1007/978-90-481-2261-5_8)
32. Kraus N, Beck A, Bolemann T, Frank H, Flad D, Gassner G, Hindenlang F, Hoffmann M, Kuhn T, Sonntag M, Munz CD (2020) FLEXI: A high order discontinuous Galerkin framework for hyperbolic-parabolic conservation laws. *Comput Math with Appl.* <https://doi.org/10.1016/j.camwa.2020.05.004>
33. Lautenschlaeger MP, Hasse H (2019) Transport properties of the Lennard-Jones truncated and shifted fluid from non-equilibrium molecular dynamics simulations. *Fluid Phase Equilib* 482:38–47. <https://doi.org/10.1016/j.fluid.2018.10.019>
34. Le Métayer O, Massoni J, Saurel R (2005) Modelling evaporation fronts with reactive Riemann solvers. *J Comput Phys* 205:567–610. <https://doi.org/10.1016/j.jcp.2004.11.021>
35. Lebon G, Jou D, Casas-Vázquez J (2008) Understanding non-equilibrium thermodynamics. Springer, Berlin. <https://doi.org/10.1007/978-3-540-74252-4>
36. Menikoff R, Plohr BJ (1989) The Riemann problem for fluid flow of real materials. *Rev Mod Phys* 61(1):75–130. <https://doi.org/10.1103/RevModPhys.61.75>
37. Merkle C, Rohde C (2007) The sharp-interface approach for fluids with phase change: Riemann problems and ghost fluid techniques. *ESAIM: Math Model Numer Anal* 41(06):1089–1123. <https://doi.org/10.1051/m2an:2007048>
38. Müller C, Hitz T, Jöns S, Zeifang J, Chiocchetti S, Munz CD (2020) Improvement of the level-set ghost-fluid method for the compressible Euler equations. In: Lamanna G, Tonini S, Cossali GE, Weigand B (eds) Droplet interaction and spray processes. Springer, Heidelberg, Berlin
39. Persson PO, Peraire J (2006) Sub-cell shock capturing for discontinuous Galerkin methods. In: 44th AIAA aerospace sciences meeting and exhibit. American Institute of Aeronautics and Astronautics. <https://doi.org/10.2514/6.2006-112>
40. Rohde C, Zeiler C (2015) A relaxation Riemann solver for compressible two-phase flow with phase transition and surface tension. *Appl Numer Math* 95:267–279. <https://doi.org/10.1016/j.apnum.2014.05.001>

41. Rohde C, Zeiler C (2018) On Riemann solvers and kinetic relations for isothermal two-phase flows with surface tension. *Z Angew Math Phys* 69(3):76. <https://doi.org/10.1007/s00033-018-0958-1>
42. Simões-Moreira JR, Shepherd JE (1999) Evaporation waves in superheated dodecane. *J Fluid Mech* 382:63–86. <https://doi.org/10.1017/S0022112098003796>
43. Sonntag M, Munz CD (2016) Efficient parallelization of a shock capturing for discontinuous Galerkin methods using finite volume sub-cells. *J Sci Comput* 70(3):1262–1289. <https://doi.org/10.1007/s10915-016-0287-5>
44. Sussman M, Smereka P, Osher S (1994) A level set approach for computing solutions to incompressible two-phase flow. *J Comput Phys* 114(1):146–159. <https://doi.org/10.1006/jcph.1994.1155>
45. Thol M, Rutkai G, Span R, Vrabec J, Lustig R (2015) Equation of state for the Lennard-Jones truncated and shifted model fluid. *Int J Thermophys* 36(1):25–43. <https://doi.org/10.1007/s10765-014-1764-4>
46. Toro EF, Spruce M, Speares W (1994) Restoration of the contact surface in the HLL-Riemann solver. *Shock Waves* 4(1):25–34. <https://doi.org/10.1007/BF01414629>
47. Zeifang J (2020) A discontinuous Galerkin method for droplet dynamics in weakly compressible flows
48. Zeiler C (2016) Liquid vapor phase transitions: modeling, Riemann solvers and computation. PhD Thesis, University of Stuttgart, Stuttgart

**Open Access** This chapter is licensed under the terms of the Creative Commons Attribution 4.0 International License (<http://creativecommons.org/licenses/by/4.0/>), which permits use, sharing, adaptation, distribution and reproduction in any medium or format, as long as you give appropriate credit to the original author(s) and the source, provide a link to the Creative Commons license and indicate if changes were made.

The images or other third party material in this chapter are included in the chapter's Creative Commons license, unless indicated otherwise in a credit line to the material. If material is not included in the chapter's Creative Commons license and your intended use is not permitted by statutory regulation or exceeds the permitted use, you will need to obtain permission directly from the copyright holder.

